

Stacking-order dependence in thermoelectric transport of biased trilayer graphene

R. Ma^{1,*}, L. Sheng^{2,†}, M. Liu³, and D. N. Sheng⁴

¹ *School of Physics and Optoelectronic Engineering,*

Nanjing University of Information Science and Technology, Nanjing 210044, China

² *National Laboratory of Solid State Microstructures and Department of Physics, Nanjing University, Nanjing 210093, China*

³ *Department of Physics, Southeast University, Nanjing 210096, China*

⁴ *Department of Physics and Astronomy, California State University, Northridge, California 91330, USA*

We numerically study the thermoelectric and thermal transport in trilayer graphene with different stacking orders in the presence of interlayer bias under a strong perpendicular magnetic field. In biased ABA-stacked case, we find that the thermoelectric conductivity displays different asymptotic behaviors with the varying of the temperature, similar to that of monolayer graphene. In the high temperature regime, the transverse thermoelectric conductivity α_{xy} saturates to a universal value $2.77k_B e/h$ at the center of each LL, while it displays a linear temperature dependence at low temperatures limit. The calculated transverse thermal conductivity κ_{xy} exhibits two plateaus away from the band center. The transition between the two plateaus is continuous, which is accompanied by a pronounced peak in the longitudinal thermal conductivity κ_{xx} . In biased ABC-stacked case, it is found that both the thermoelectric conductivity and thermal conductivity have similar properties to the biased bilayer graphene, which is consistent with the behavior of a band insulator. The obtained results demonstrate the sensitivity of the thermoelectric conductivity to the band gap near the Dirac point. We also verify the validity of the Mott-relation and the generalized Wiedemann-Franz law.

PACS numbers: 72.80.Vp; 72.10.-d; 73.50.Lw, 73.43.Cd

I. INTRODUCTION

Recently, much attention has been paid to the thermoelectric transport properties of graphene both experimentally¹⁻³ and theoretically⁴⁻⁸. In experiments, the thermopower (the longitudinal thermoelectric response) and the Nernst signal (the transverse response) in the presence of a strong magnetic field are found to be large, reaching the order of the quantum limit k_B/e , where k_B and e are the Boltzmann constant and the electron charge, respectively¹⁻³. Besides monolayer graphene, bilayer graphene is also very interesting. Experiments have shown that bilayer graphene exhibits tunable bandgap^{9,10} in the presence of an applied bias voltage, exhibiting similar properties to semiconductors. Thermoelectric measurement¹¹ shows that the room-temperature thermopower with a bias voltage can be enhanced by a factor of 4 compared to that of the monolayer graphene or unbiased bilayer graphene, making it a more promising candidate for future thermoelectric applications. Theoretical calculations from the tight-binding models for monolayer and bilayer graphene^{12,13} are in agreement with the experimental observations^{1-3,11,14}.

More recently, the focus of the study of graphene systems has gradually extended to trilayer graphene¹⁵⁻²². In trilayer graphene, the interlayer coupling in stacked layers of graphene gives rise to even richer electronic transport properties. Experimental and theoretical studies show that²³⁻²⁶, the electronic structure and the Landau level (LL) spectrum at the vicinity of the Dirac point are very sensitive to the stacking order of the graphene layers. Trilayer graphene has two stable stacking orders: (1) ABA (Bernal) stacking, where the atoms of the top-most layer lie exactly on top of those of the bottom layer;

and (2) ABC (rhombohedral) stacking, where atoms of one sublattice of the top layer lie above the center of the hexagons in the bottom layer. This seemingly small distinction in stacking order results in a dramatic difference in band structures. The low-energy band structure for ABA-stacked trilayer graphene contains both linear and hyperbolic bands, similar to the combined spectrum of monolayer graphene and bilayer graphene^{27,28}, while ABC-stacked case presents approximately cubic bands²⁵. Moreover, the LL spectrum of ABA-stacked case in a perpendicular magnetic field B can be viewed as a superposition of \sqrt{B} -dependent monolayer-like LLs and B -dependent bilayer-like LLs^{23,29,30}. On the other hand, the LLs of ABC-stacked case are given by $E_n \propto B^{3/2} \sqrt{n(n-1)(n-2)}$ with Berry's phase 3π ²³⁻²⁵. Interestingly, when a bias voltage or a potential difference is applied to the top and bottom graphene layers, ABA-stacked case exhibits a semi-metallic band structure with a tunable band overlap between the conduction and valence bands^{31,32}, whereas ABC-stacked case exhibits a semiconducting band structure with a tunable band gap, similarly to bilayer graphene^{23,25,26,33}. Owing to their distinctive band structures, ABA- and ABC-stacked trilayer graphene are expected to exhibit rich novel thermoelectric transport properties. However, theoretical understanding of the thermoelectric transport properties of trilayer graphene is limited compared to that of monolayer or bilayer graphene. In particular, the influence of different stacking orders on the thermoelectric transport properties has not been studied so far, which is highly desired.

In this paper, we carry out a numerical study of the thermoelectric transport properties in both ABA- and ABC-stacked trilayer graphene systems in the presence of

electrostatic bias between the top and bottom graphene layers. The effects of disorder and thermal activation on the broadening of LLs are considered. In biased ABA-stacked case, the thermoelectric coefficients exhibit unique characteristics near the central LL due to the LL crossing of electron and hole bands, which are quite different from those of biased bilayer graphene. Both the longitudinal and the transverse thermoelectric conductivities are universal functions of the effective bandwidth and temperature, and display different asymptotic behaviors in different temperature regimes. The Nernst signal displays a peak at the central LL with a height of the order of k_B/e , and changes sign near other LLs, while the thermopower behaves in an opposite manner. The peak values of the Nernst signal and thermopower are very large, compared with monolayer graphene due to the semi-metallic band overlap near zero energy. The validity of the semiclassical Mott relation is found to remain valid at low temperatures. In biased ABC-stacked case, we observe quite different behavior from biased ABA-stacked case near the central LL. Around the Dirac point, the transverse thermoelectric conductivity exhibits a pronounced valley at low temperatures. This is attributed to the opening of a sizable gap between the valence and conduction bands in biased ABC-stacked case. In addition, we have calculated the thermal transport coefficients of electrons for both biased ABA- and ABC-stacked trilayer graphene systems. In biased ABA-stacked case, the calculated transverse thermal conductivity κ_{xy} exhibits two plateaus away from the band center. The transition between the two plateaus is continuous, which is accompanied by a pronounced peak in the longitudinal thermal conductivity κ_{xx} . In biased ABC-stacked case, the transverse thermal conductivity κ_{xy} displays an apparent plateau with $\kappa_{xy} = 0$, which is accompanied by a valley in κ_{xx} , which provides an additional evidence for the band insulator behavior. We further compare the calculated thermal conductivities with those deduced from the Wiedemann-Franz law, to check the validity of this fundamental relation in trilayer graphene systems.

This paper is organized as follows. In Sec. II, we introduce the model Hamiltonian. In Sec. III and Sec. IV, numerical results based on exact diagonalization and thermoelectric transport calculations are presented for biased ABA-stacked and ABC-stacked trilayer graphene systems, respectively. In Sec. V, numerical results for thermal transport coefficients are presented. The final section contains a summary.

II. MODEL AND METHODS

We consider a trilayer graphene system consisting of three coupled hexagonal lattices including inequivalent sublattices A_1, B_1 on the bottom layer, A_2, B_2 on the middle layer, and A_3, B_3 on the top layer. The three graphene layers are arranged in the ABA (Bernal) or ABC (rhombohedral) stacking orders³⁴, as shown in

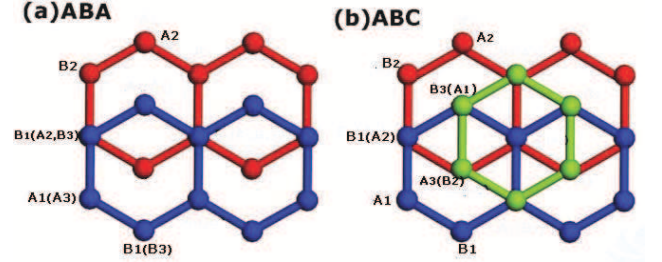


FIG. 1: (color online). Schematic of trilayer graphene lattice with ABA and ABC stacking, where the blue/red/green lines indicate links on the bottom/middle/top layers.

Fig.1. The difference between ABA and ABC stacking is the top layer. For ABA stacking, the top layer will be exactly above the bottom layer without any relative shift. For ABC stacking, A_3 sublattice of the top layer lies above the centers of the hexagons in the bottom layer, B_3 sublattice lies above the centers of the hexagons in the middle layer. Here, the in-plane nearest-neighbor hopping integral between A_i and B_i atoms is denoted by $\gamma_{A_i B_i} = \gamma_0$ with $i = 1, \dots, 3$. For the interlayer coupling, we take into account two largest hopping integrals. For ABA stacking, the largest interlayer hopping is between a B_1 (B_3) atom and the nearest A_2 atom $\gamma_{B_1 A_2} = \gamma_{B_3 A_2} = \gamma_1$. The smaller hopping is between a B_2 atom and three nearest A_1 (A_3) atoms $\gamma_{B_2 A_1} = \gamma_{B_2 A_3} = \gamma_3$. For ABC stacking, the largest interlayer hopping is between a B_1 (B_2) atom and the nearest A_2 (A_3) atom $\gamma_{B_1 A_2} = \gamma_{B_2 A_3} = \gamma_1$. The smaller hopping is between a B_2 (B_3) atom and three nearest A_1 (A_2) atoms $\gamma_{B_2 A_1} = \gamma_{B_3 A_2} = \gamma_3$. The values of these hopping integrals are taken to be $\gamma_0 = 3.16$ eV, $\gamma_1 = 0.39$ eV, and $\gamma_3 = 0.315$ eV³⁵.

We assume that each monolayer graphene has totally L_y zigzag chains with L_x atomic sites on each zigzag chain³⁶. The size of the sample will be denoted as $N = L_x \times L_y \times L_z$, where $L_z = 3$ is the number of monolayer graphene planes along the z direction. We have confirmed that the calculated results does not depend on the system sizes (as long as the system lengths are reasonably large)³⁵. In the presence of an applied magnetic field perpendicular to the plane of biased trilayer graphene, the lattice model for ABA stacking in real space can be written in the tight-binding form:

$$\begin{aligned}
 H = & -\gamma_0 \left(\sum_{\langle ij \rangle \sigma} e^{ia_{ij}} c_{1i\sigma}^\dagger c_{1j\sigma} + \sum_{\langle ij \rangle \sigma} e^{ia_{ij}} c_{2i\sigma}^\dagger c_{2j\sigma} \right. \\
 & + \sum_{\langle ij \rangle \sigma} e^{ia_{ij}} c_{3i\sigma}^\dagger c_{3j\sigma} \left. - \gamma_1 \left(\sum_{\langle ij \rangle 1\sigma} e^{ia_{ij}} c_{1j\sigma B_1}^\dagger c_{2i\sigma A_2} \right. \right. \\
 & + \sum_{\langle ij \rangle 1\sigma} e^{ia_{ij}} c_{3j\sigma B_3}^\dagger c_{2i\sigma A_2} \left. - \gamma_3 \left(\sum_{\langle ij \rangle 3\sigma} e^{ia_{ij}} c_{2j\sigma B_2}^\dagger c_{1i\sigma A_1} \right. \right. \\
 & \left. \left. + \sum_{\langle ij \rangle 3\sigma} e^{ia_{ij}} c_{2j\sigma B_2}^\dagger c_{3i\sigma A_3} \right) + h.c. \right) + \sum_{i\sigma} w_i (c_{1i\sigma}^\dagger c_{1i\sigma}
 \end{aligned}$$

$$+ c_{2i\sigma}^\dagger c_{2i\sigma} + c_{3i\sigma}^\dagger c_{3i\sigma} + \sum_{i\sigma} (\epsilon_1 c_{1i\sigma}^\dagger c_{1i\sigma} + \epsilon_2 c_{3i\sigma}^\dagger c_{3i\sigma}) \quad (1)$$

where $c_{mi\sigma}^\dagger$ ($c_{mi\sigma}^\dagger c_{mi\sigma A_m}$), $c_{mj\sigma}^\dagger$ ($c_{mj\sigma}^\dagger c_{mj\sigma B_m}$) are creation operators on A_m and B_m sublattices in the m -th layer ($m = 1, \dots, 3$), with σ as a spin index. The sum $\sum_{\langle ij \rangle \sigma}$ denotes the intralayer nearest-neighbor hopping in three layers, $\sum_{\langle ij \rangle_{1\sigma}}$ stands for the interlayer hopping between the B_1 (B_3) sublattice in the bottom (top) layer and the A_2 sublattice in the middle layer, and $\sum_{\langle ij \rangle_{3\sigma}}$ stands for the interlayer hopping between the B_2 sublattice in the middle layer and the A_1 (A_3) sublattice in the bottom (top) layer, as described above. For the biased system, the top and the bottom graphene layers gain different electrostatic potentials, and the corresponding energy difference is given by $\Delta_g = \epsilon_2 - \epsilon_1$ where $\epsilon_1 = -\frac{1}{2}\Delta_g$, and $\epsilon_2 = \frac{1}{2}\Delta_g$. For illustrative purpose, a relatively large asymmetric gap $\Delta_g = 0.3\gamma_0$ is assumed. w_i is a random disorder potential uniformly distributed in the interval $w_i \in [-W/2, W/2]\gamma_0$. The magnetic flux per hexagon $\phi = \sum_{\square} a_{ij} = \frac{2\pi}{M}$ is proportional to the strength of the applied magnetic field B , where M is assumed to be an integer and the lattice constant is taken to be unity.

For ABC-stacked trilayer graphene in the presence of bias voltage, the Hamiltonian can be written as:

$$\begin{aligned} H = & -\gamma_0 \left(\sum_{\langle ij \rangle \sigma} e^{ia_{ij}} c_{1i\sigma}^\dagger c_{1j\sigma} + \sum_{\langle ij \rangle \sigma} e^{ia_{ij}} c_{2i\sigma}^\dagger c_{2j\sigma} \right. \\ & + \sum_{\langle ij \rangle \sigma} e^{ia_{ij}} c_{3i\sigma}^\dagger c_{3j\sigma} \left. \right) - \gamma_1 \left(\sum_{\langle ij \rangle_{1\sigma}} e^{ia_{ij}} c_{1j\sigma B_1}^\dagger c_{2i\sigma A_2} \right. \\ & + \sum_{\langle ij \rangle_{1\sigma}} e^{ia_{ij}} c_{2j\sigma B_2}^\dagger c_{3i\sigma A_3} \left. \right) - \gamma_3 \left(\sum_{\langle ij \rangle_{3\sigma}} e^{ia_{ij}} c_{2j\sigma B_2}^\dagger c_{1i\sigma A_1} \right. \\ & + \sum_{\langle ij \rangle_{3\sigma}} e^{ia_{ij}} c_{3j\sigma B_3}^\dagger c_{2i\sigma A_2} \left. \right) + h.c. + \sum_{i\sigma} w_i (c_{1i\sigma}^\dagger c_{1i\sigma} \\ & + c_{2i\sigma}^\dagger c_{2i\sigma} + c_{3i\sigma}^\dagger c_{3i\sigma}) + \sum_{i\sigma} (\epsilon_1 c_{1i\sigma}^\dagger c_{1i\sigma} + \epsilon_2 c_{3i\sigma}^\dagger c_{3i\sigma}) \quad (2) \end{aligned}$$

The sum $\sum_{\langle ij \rangle \sigma}$ denotes the intralayer nearest-neighbor hopping in three layers, $\sum_{\langle ij \rangle_{1\sigma}}$ stands for the interlayer hopping between the B_1 (B_2) sublattice in the bottom (middle) layer and the A_2 (A_3) sublattice in the middle (top) layer, and $\sum_{\langle ij \rangle_{3\sigma}}$ stands for the interlayer hopping between the B_2 (B_3) sublattice in the middle (top) layer and the A_1 (A_2) sublattice in the bottom (middle) layer, as described above.

In the linear response regime, the charge current in response to an electric field and a temperature gradient can be written as $\mathbf{J} = \hat{\sigma} \mathbf{E} + \hat{\alpha}(-\nabla T)$, where $\hat{\sigma}$ and $\hat{\alpha}$ are the electrical and thermoelectric conductivity tensors, respectively. The transport coefficient σ_{xx} can be calculated by Kubo formula and σ_{xx} can be obtained based on the calculation of the Thouless number³⁵. In practice, we first calculate the $T = 0$ conductivities $\sigma_{ji}(E_F)$, and then use the relation³⁷

$$\sigma_{ji}(E_F, T) = \int d\epsilon \sigma_{ji}(\epsilon) \left(-\frac{\partial f(\epsilon)}{\partial \epsilon} \right),$$

$$\alpha_{ji}(E_F, T) = \frac{-1}{eT} \int d\epsilon \sigma_{ji}(\epsilon) (\epsilon - E_F) \left(-\frac{\partial f(\epsilon)}{\partial \epsilon} \right) \quad (3)$$

to obtain the finite-temperature electrical and thermoelectric conductivity tensors. Here, $f(x) = 1/[e^{(x-E_F)/k_B T} + 1]$ is the Fermi distribution function. At low temperatures, the second equation can be approximated as

$$\alpha_{ji}(E_F, T) = -\frac{\pi^2 k_B^2 T}{3e} \frac{d\sigma_{ji}(\epsilon, T)}{d\epsilon} \Big|_{\epsilon=E_F}, \quad (4)$$

which is the semiclassical Mott relation^{37,38}. The thermopower and Nernst signal can be calculated subsequently from³⁹

$$\begin{aligned} S_{xx} &= \frac{E_x}{\nabla_x T} = \rho_{xx} \alpha_{xx} - \rho_{yx} \alpha_{yx}, \\ S_{xy} &= \frac{E_y}{\nabla_x T} = \rho_{xx} \alpha_{yx} + \rho_{yx} \alpha_{xx}. \end{aligned} \quad (5)$$

The thermal conductivity, measuring the magnitude of the thermal currents in response to an applied temperature gradient, which usually includes electron and phonon contributions. In our numerical calculations, phonon-related thermal conductivity is omitted. The electronic thermal conductivities κ_{ji} at finite temperature assume the forms³⁸

$$\begin{aligned} \kappa_{ji}(E_F, T) &= \frac{1}{e^2 T} \int d\epsilon \sigma_{ji}(\epsilon) (\epsilon - E_F)^2 \left(-\frac{\partial f(\epsilon)}{\partial \epsilon} \right) \\ &- T \alpha_{ji}(E_F, T) \sigma_{ji}^{-1}(E_F, T) \alpha_{ji}(E_F, T). \end{aligned} \quad (6)$$

For diffusive electronic transport in metals, it is established that the Wiedemann-Franz law is satisfied between the electrical conductivity σ and the thermal conductivity κ of electrons⁴⁰:

$$\frac{\kappa}{\sigma T} = L, \quad (7)$$

where L is the Lorentz number and takes a constant value: $L = \frac{\pi^2}{3} \left(\frac{k_B}{e} \right)^2$. The validity of this relation will be examined for the present trilayer graphene.

III. THERMOELECTRIC TRANSPORT IN BIASED ABA-STACKED TRILAYER GRAPHENE SYSTEMS

We first show the calculated thermoelectric conductivities at finite temperatures for biased ABA-stacked trilayer graphene. As shown in Fig.2(a) and (b), the transverse thermoelectric conductivity α_{xy} displays a series of peaks, while the longitudinal thermoelectric conductivity α_{xx} oscillates and changes sign at the center of each LL. At low temperatures, the peak of α_{xy} at the central LL is higher and narrower than others, which indicates that the impurity scattering has less effect on the central LL. These results are qualitatively similar to those found

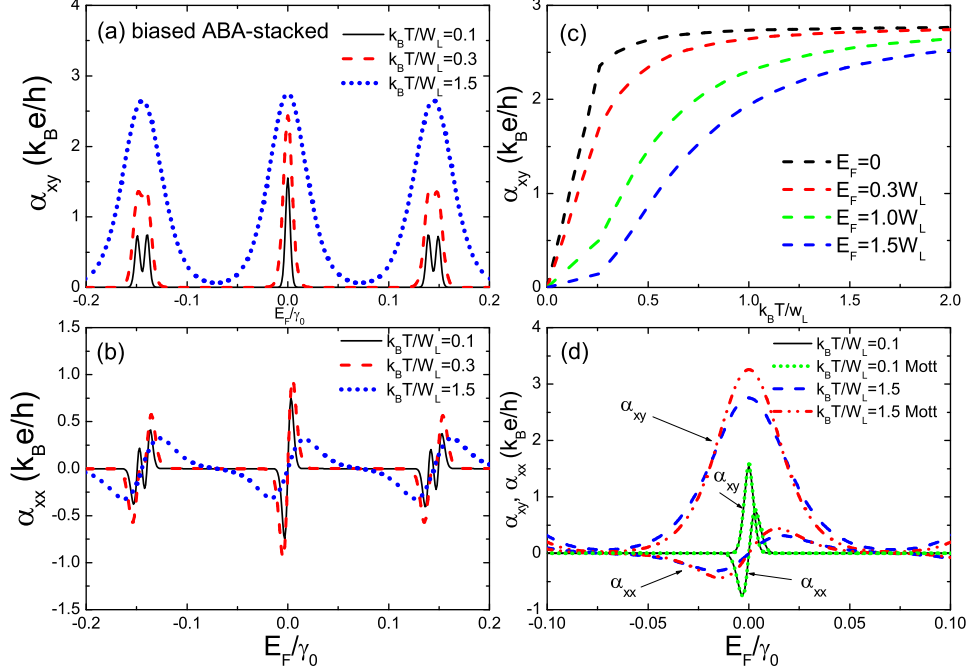


FIG. 2: (color online). Thermoelectric conductivities at finite temperatures of biased ABA-stacked trilayer graphene. (a)-(b) $\alpha_{xy}(E_F, T)$ and $\alpha_{xx}(E_F, T)$ as functions of the Fermi energy E_F at different temperature T . (c) shows the temperature dependence of $\alpha_{xy}(E_F, T)$ for trilayer graphene. (d) Comparison of the results from numerical calculations and from the generalized Mott relation at two characteristic temperatures, $k_B T/W_L = 0.1$ and $k_B T/W_L = 1.5$. Here, the width of the central LL $W_L/\gamma_0 = 0.0069$. The asymmetric gap $\Delta_g = 0.3\gamma_0$. The system size is taken to be $N = 96 \times 24 \times 3$, the magnetic flux $\phi = 2\pi/48$, and the disorder strength $w = 0.1$.

in monolayer graphene, but some differences exist due to the overlap of electron and hole bands. At low temperatures, more oscillations are observed in the higher LLs than monolayer graphene, in consistent with the further lifting of the LL degeneracy in biased ABA-stacked case. As shown in Fig.2(b), around zero energy, the peak value of α_{xx} shows different trends with increasing temperature. It first increases with T in the low-temperature region, and then decreases with T at high temperatures. This is due to the competition between $\frac{\pi^2 k_B^2 T}{3e}$ and $\frac{d\sigma_{ji}(\epsilon, T)}{d\epsilon}$ of Eq.(4). The peak value of α_{xx} could either increase or decrease depending on the relative magnitudes of these two terms. At high temperatures, $\sigma_{ji}(\epsilon, T)$ becomes smooth, and consequently α_{xx} begins to decrease. In Fig.2(c), we find that α_{xy} shows different behavior depending on the relative strength of the temperature $k_B T$ and the width of the central LL W_L (W_L is determined by the full-width at the half-maximum of the σ_{xx} peak). When $k_B T \ll W_L$ and $E_F \ll W_L$, α_{xy} shows linear temperature dependence, indicating that there is a small energy range where extended states dominate, and the transport falls into the semi-classical Drude-Zener regime. When E_F is shifted away from the Dirac point,

the low-energy electron excitation is gapped due to Anderson localization. When $k_B T$ becomes comparable to or greater than W_L , α_{xy} for all LLs saturates to a constant value $2.77k_B e/h$. This matches exactly the universal value $(\ln 2)k_B e/h$ predicted for the conventional integer quantum Hall effect (IQHE) systems in the case where thermal activation dominates^{37,38}, with an additional degeneracy factor 4. The saturated value of α_{xy} in biased ABA-stacked case is in accordance with the four-fold degeneracy at zero energy. In the presence of bias voltage, the valley degeneracy of the LLs usually is lifted by the interlayer potential asymmetry, so that the 12-fold energy levels (four and eight levels from the monolayer-like and the bilayer-like subbands, respectively) split into six different levels with twofold spin degeneracy. However, near the Dirac point, the interlayer potential asymmetry causes hybridization of the linear and parabolic chiral bands, which leads to the fourfold degeneracy for zero energy Landau levels.^{20–22}

To examine the validity of the semiclassical Mott relation, we compare the above results with those calculated from Eq.(4), as shown in Fig.2(d). The Mott relation is a low-temperature approximation and predicts that the thermoelectric conductivities have linear temperature de-

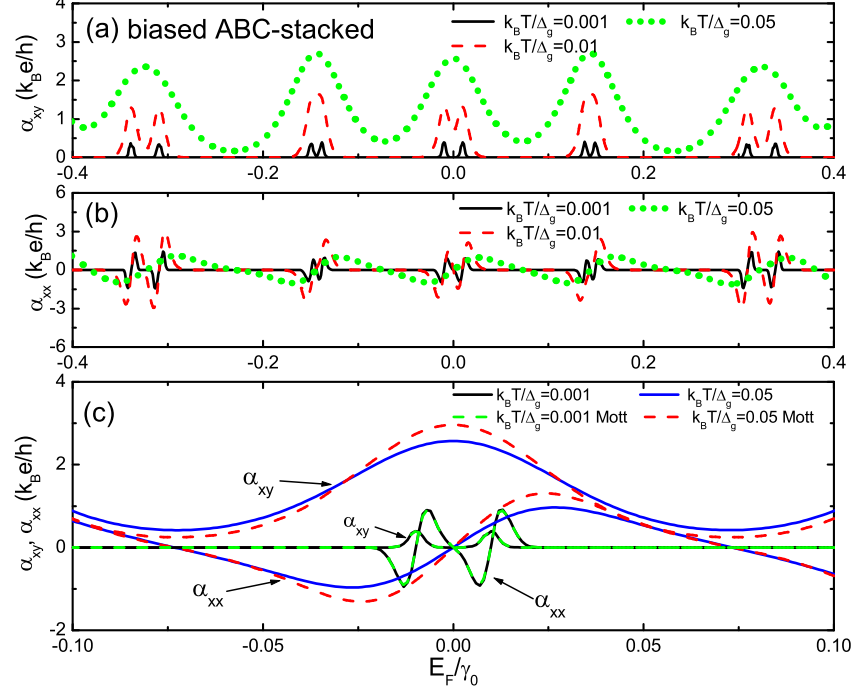


FIG. 3: (color online). Thermoelectric conductivities at finite temperatures of biased ABC-stacked trilayer graphene. (a)-(b) $\alpha_{xy}(E_F, T)$ and $\alpha_{xx}(E_F, T)$ as functions of Fermi energy at different temperatures. (c) Comparison of the results from numerical calculations and from the generalized Mott relation at two characteristic temperatures, $k_B T/\Delta_g = 0.001$ and $k_B T/\Delta_g = 0.05$. The asymmetric gap $\Delta_g = 0.3\gamma_0$. The other parameters are chosen to be the same as in Fig. 2.

pendence. This is in agreement with our low-temperature results, which proves that the semiclassical Mott relation is asymptotically valid in the Landau-quantized systems, as suggested in Ref. 37.

IV. THERMOELECTRIC TRANSPORT IN BIASED ABC-STACKED TRILAYER GRAPHENE SYSTEMS

For biased ABC-stacked trilayer graphene, we show the calculated α_{xx} and α_{xy} at finite temperatures in Fig. 3. As seen from Fig. 3(a), α_{xy} displays a pronounced valley at low temperature, in striking contrast to ABA-stacked case with a peak at $E_F = 0$. These results are qualitatively similar to those found in biased bilayer graphene¹³. This behavior can be understood as due to the split of the valley degeneracy in the central LL by an opposite voltage bias added to the top layer and the bottom layer. This is in consistent with the opening of a sizable gap between the valence and conduction bands in biased ABC-stacked trilayer graphene⁴¹. α_{xx} oscillates and changes sign around the center of each split LL. In Fig. 2(c), we also compare the above results with those calculated from the semiclassical Mott relation using Eq. (4). The Mott

relation is found to remain valid at low temperatures.

We further calculate the thermopower S_{xx} and the Nernst signal S_{xy} . In Fig. 4(a)-(b), we show the calculated S_{xx} and S_{xy} in biased ABA-stacked trilayer graphene. As we can see, S_{xy} (S_{xx}) has a peak (peaks) at the central LL (the other LLs), and changes sign near the other LLs (the central LL). At zero energy, both ρ_{xy} and α_{xx} vanish, leading to a vanishing S_{xx} . Around zero energy, because $\rho_{xx}\alpha_{xx}$ and $\rho_{xy}\alpha_{xy}$ have opposite signs, depending on their relative magnitudes, S_{xx} could either increases or decreases when E_F is increased passing the Dirac point. In biased ABA-stacked case, S_{xx} is dominated by $\rho_{xy}\alpha_{xy}$, consequently, S_{xx} increases to positive value as E_F passing zero. At low temperatures, the peak value of S_{xx} near zero energy is $\pm 0.81 k_B/e$ ($\pm 69.8 \mu\text{V/K}$) at $k_B T = 0.4 W_L$, which is in agreement with the measured value ($\pm 70 \mu\text{V/K}$).⁴² With the increase of temperature, the peak height increases to $\pm 3.75 k_B/e$ ($\pm 323.14 \mu\text{V/K}$) at $k_B T = 1.5 W_L$. On the other hand, S_{xy} has a strong peak structure around zero energy, which is dominated by $\rho_{xx}\alpha_{xy}$. The peak height is $7.82 k_B/e$ ($673.85 \mu\text{V/K}$) at $k_B T = 1.5 W_L$. The large magnitude of S_{xy} and S_{xx} near zero energy can be attributed to the semi-metal type dispersion of biased ABA-stacked trilayer graphene, and the fact that the system is in the

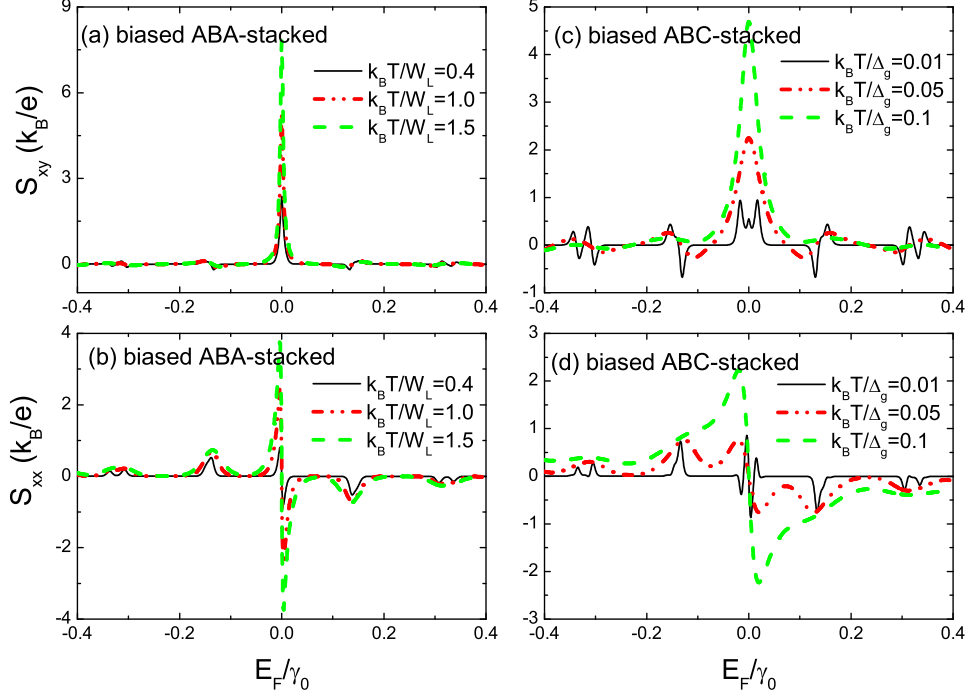


FIG. 4: (color online). The thermopower S_{xx} and the Nernst signal S_{xy} as functions of the Fermi energy in (a)-(b) biased ABA-stacked trilayer graphene, and (c)-(d) biased ABC-stacked trilayer graphene at different temperatures. The parameters in these two systems are chosen to be the same as in Fig. 2 and Fig. 3, respectively.

vicinity of a quantum Hall liquid to insulator transition, where the imbalance between the particle and hole types of carriers should be significant. The thermoelectric effects are very sensitive to such an imbalance in Dirac materials in comparison with conventional metals.

In Fig.4(c)-(d), we show the calculated S_{xx} and S_{xy} in biased ABC-stacked case. As we can see, S_{xy} (S_{xx}) has a peak (peaks) around zero energy (the other LLs), and changes sign near the other LLs (zero energy). These results are qualitatively similar to those found in biased ABA-stacked case. In our calculation, we find that S_{xx} is always dominated by $\rho_{xx}\alpha_{xx}$, consequently, S_{xx} decreases to negative values as E_F passing zero. This is different from biased ABA-stacked case. At low temperatures, the peak value of S_{xx} near zero energy is $\pm 0.86k_B/e$ ($\pm 74.11 \mu\text{V/K}$) at $k_B T = 0.01\Delta_g$. With the increase of temperature, the peak height increases to $\pm 2.23k_B/e$ ($\pm 192.16 \mu\text{V/K}$) at $k_B T = 0.1\Delta_g$. On the other hand, S_{xy} has a peak structure around zero energy, which is dominated by $\rho_{xy}\alpha_{xx}$. The peak height is $4.69k_B/e$ ($404.14 \mu\text{V/K}$) at $k_B T = 0.1\Delta_g$.

V. THERMAL CONDUCTIVITY IN BIASED ABA- AND ABC-STACKED TRILAYER GRAPHENE SYSTEMS

We now focus on thermal conductivities. In Fig. 5, we show results of the transverse thermal conductivity κ_{xy} and the longitudinal thermal conductivity κ_{xx} for biased ABA-stacked trilayer graphene at different temperatures. As seen from Fig.5(a) and (b), κ_{xy} exhibits two flat plateaus away from the central LL. The values of the plateaus in κ_{xy} are $\pm 0.0045\gamma_0 k_B/h$ ($\pm 0.048 \text{ nW/(K}\cdot\text{m)}$) at $k_B T = 0.1W_L$. With the increase of temperature, the values of the plateaus increase to $\pm 0.023\gamma_0 k_B/h$ ($\pm 0.24 \text{ nW/(K}\cdot\text{m)}$) at $k_B T = 0.5W_L$. At low temperatures, the transition between these two plateaus is smooth and monotonic, while at higher temperatures, κ_{xy} exhibits an oscillatory feature at $k_B T = 0.5W_L$ between two plateaus. On the other hand, κ_{xx} displays a peak near the center LL, and its peak value increases quickly with T . The peak height is $0.028\gamma_0 k_B/h$ ($0.3 \text{ nW/(K}\cdot\text{m)}$) at $k_B T = 0.5W_L$. To test the validity of the Wiedemann-Franz Law, we compare the above results with those calculated from Eq.(7), as shown in Fig.5(c) and (d). The Wiedemann-Franz Law predicts that the ratio of the thermal conductivity κ to the electrical conductivity σ of a metal is proportional to the temperature. This

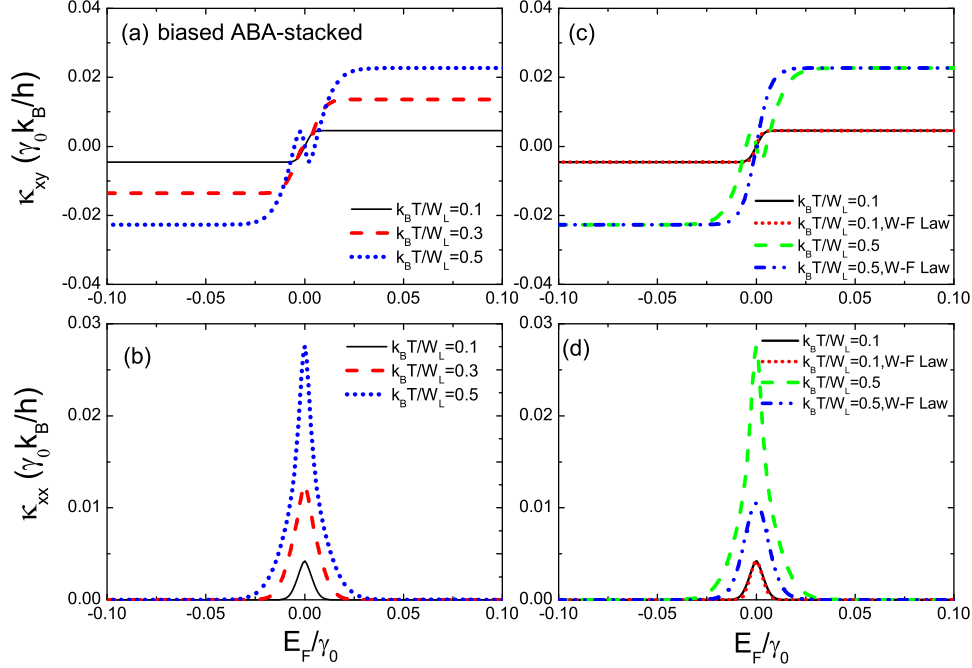


FIG. 5: (color online). (a)-(b) Thermal conductivities $\kappa_{xy}(E_F, T)$ and $\kappa_{xx}(E_F, T)$ as functions of the Fermi energy in biased ABA-stacked trilayer graphene at different temperatures. (c)-(d) Comparison between the thermal conductivity as functions of the Fermi energy from numerical calculations and from the Wiedemann-Franz Law at two characteristic temperatures. The parameters used here are the same as in Fig.2.

is in agreement with our low-temperature results, but apparent deviation is seen at higher temperatures.

In Fig. 6, we show the calculated thermal conductivities κ_{xx} and κ_{xy} for biased ABC-stacked case. As seen from Fig.6(a) and (b), around zero energy, a flat region with $\kappa_{xy} = 0$ is found at low temperatures, which is accompanied by a valley in κ_{xx} . These features are clearly in contrast to those of ABA-stacked case due to the presence of an energy gap between the valence and conduction bands. When temperature increases to $k_B T = 0.06\Delta_g$, the plateau with $\kappa_{xy} = 0$ disappears, while κ_{xx} displays a large peak. The peak height κ_{xx} is $0.14\gamma_0 k_B/h$ ($1.49 \text{ nW}/(\text{K}\cdot\text{m})$) at $k_B T = 0.06\Delta_g$. In Fig.6(c) and (d), we also compare the above results with those calculated from the Wiedemann-Franz Law using Eq.(7). We find that the Wiedemann-Franz Law remain valid at low temperatures.

VI. SUMMARY

In summary, we have numerically investigated the thermoelectric and thermal transport properties of biased trilayer graphene with different stacking orders in the presence of both disorder and a strong magnetic field. In biased ABA-stacked case, the thermoelectric coefficients

exhibit unique characteristics due to the LL crossing of electron and hole bands that are strongly suggestive of a semi-metallic band overlap. We find that the thermoelectric conductivities display different asymptotic behavior depending on the ratio between the temperature and the width of the disorder-broadened LLs, similar to those found in monolayer graphene. In the high temperature regime, the transverse thermoelectric conductivity α_{xy} saturates to a universal value $2.77k_B e/h$ at the center of each LL, and displays a linear temperature dependence at low temperatures. The calculated Nernst signal S_{xy} shows a strong peak at the central LL with heights of the order of k_B/e , and changes sign at the other LLs, while the thermopower S_{xx} has an opposite behavior. The calculated transverse thermal conductivity κ_{xy} exhibits two plateaus away from the band center. The transition between these two plateaus is continuous, which is accompanied by a pronounced peak in longitudinal thermal conductivity κ_{xx} . The validity of the Wiedemann-Franz law relating the thermal conductivity κ and the electrical conductivity σ is verified to be valid only at very low temperatures.

In biased ABC-stacked case, the thermoelectric coefficients display quite distinct behaviors from those of ABA-stacked case. Around the Dirac point, the transverse thermoelectric conductivity α_{xy} exhibits a pro-

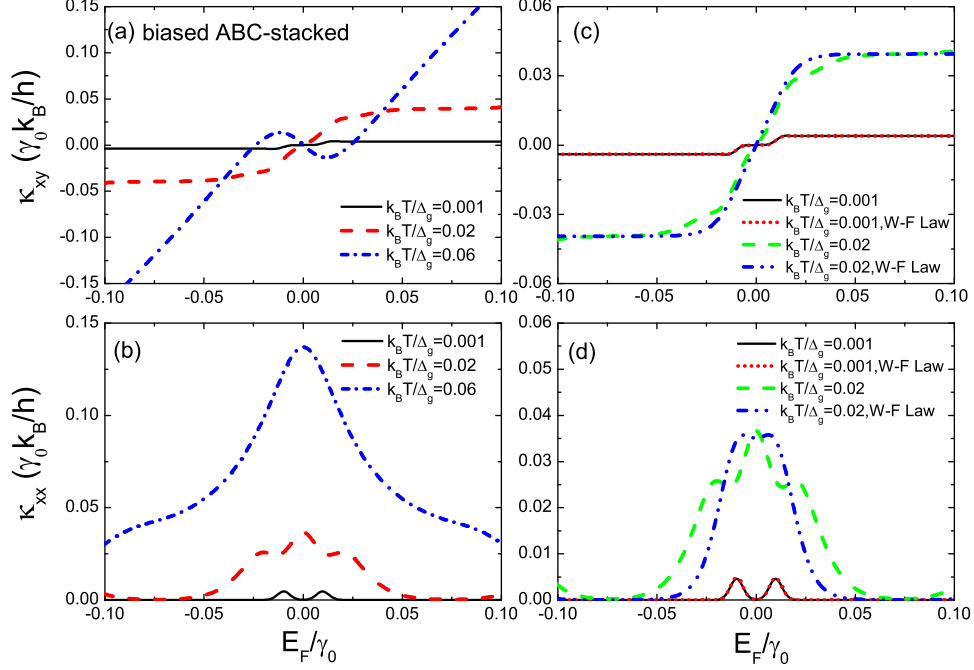


FIG. 6: (color online). (a)-(b) Thermal conductivities $\kappa_{xy}(E_F, T)$ and $\kappa_{xx}(E_F, T)$ as functions of the Fermi energy in biased ABC-stacked trilayer graphene at different temperatures, (c)-(d) Comparison between the thermal conductivity as functions of the Fermi energy obtained from numerical calculations and from the Wiedemann-Franz Law at two characteristic temperatures. The parameters chosen here are the same as in Fig.3.

nounced valley with $\alpha_{xy} = 0$ at low temperatures, in striking contrast to ABA-stacked case with a peak. The validity of the semiclassical Mott relation between the thermoelectric and electrical transport coefficients is verified to be satisfied only at very low temperatures. Furthermore, the transverse thermal conductivity κ_{xy} has a pronounced plateau with $\kappa_{xy} = 0$, which is accompanied by a valley in κ_{xx} . These are consistent with the opening of sizable gap between the valence and conductance bands in biased ABC-stacked case.

We mention that in our numerical calculations, the flux $2\pi/M$ in each hexagon gives a magnetic field of the strength $B \sim 1.3 \times 10^5/M$ Tesla⁴³. Thus the magnetic field B we used is about 2700 Tesla. This magnetic field is much stronger than the ones which can be achieved in the experimental situation, as limited by current computational capability. In our calculation, the system size is taken to be $N = 96 \times 24 \times 3$, and M is taken to be L_x or L_y

in consistence with periodic boundary conditions, which limits us to extremely strong magnetic fields. However, the obtained thermoelectric transport coefficients exhibit universal behaviors, as long as M is not too small (greater than 10).

Acknowledgments

This work is supported by Scientific Research Foundation of Nanjing University of Information and Technology of China under Grant No. 20100401, the NSFC Grant No. 11104146 (RM), the NSFC Grant No. 11074110, the National Basic Research Program of China under Grant No 2009CB929504 (LS). We also thank the US NSF Grants DMR-0906816 and DMR-1205734 (DNS), Princeton MRSEC Grant DMR-0819860 for travel support, and the NSF instrument grant DMR-0958596 (DNS).

* Electronic address: njrma@hotmail.com

† Electronic address: shengli@nju.edu.cn

¹ Y. M. Zuev, W. Chang, and P. Kim, Phys. Rev. Lett. **102**, 096807 (2009).

² P. Wei, W. Bao, Y. Pu, C. N. Lau, and J. Shi, Phys. Rev. Lett. **102**, 166808 (2009).

³ J. G. Checkelsky and N. P. Ong, Phys. Rev. B **80**, 081413(R) (2009).

- ⁴ A. H. Castro Neto, F. Guinea, N. M. R. Peres, K. S. Novoselov and A. K. Geim, Rev. Mod. Phys. **81**, 109 (2009).
- ⁵ E. H. Hwang, E. Rossi, and S. Das Sarma, Phys. Rev. B **80**, 235415 (2009).
- ⁶ T. Löfwander and M. Fögelstrom, Phys. Rev. B **76**, 193401 (2007).
- ⁷ B. Dóra and P. Thalmeier, Phys. Rev. B **76**, 035402 (2007).
- ⁸ X. Z. Yan, Y. Romiah, and C. S. Ting, Phys. Rev. B **80**, 165423 (2009).
- ⁹ Y. Zhang, T. T. Tang, C. Girit, Z. Hao, M. C. Martin, A. Zettl, M. F. Crommie, Y. R. Shen, F. Wang, Nature **459**, 820 (2009).
- ¹⁰ A. B. Kuzmenko, I. Crassee, D. van der Marel, P. Blake, K. S. Novoselov, Phys. Rev. B **80**, 165406 (2009).
- ¹¹ L. Hao and T. K. Lee, Phys. Rev. B **81**, 165445 (2010).
- ¹² L. Zhu, R. Ma, L. Sheng, M. Liu, and D. N. Sheng, Phys. Rev. Lett. **104**, 076804 (2010).
- ¹³ R. Ma, L. Zhu, L. Sheng, M. Liu, and D. N. Sheng, Phys. Rev. B **84**, 075420 (2011).
- ¹⁴ S. G. Nam, D. K. Ki, H. J. Lee, Phys. Rev. B **82**, 245416 (2010).
- ¹⁵ T. Taychatanapat, K. Watanabe, T. Taniguchi and P. J. Herrero, Nature Physics **7**, 621 (2011).
- ¹⁶ L. Y. Zhang, Y. Zhang, J. Camacho, M. Khodas and I. Zalitznyak, Nature Physics **7**, 953 (2011).
- ¹⁷ A. Kumar, W. Escoffier, J. M. Poumiro, C. Faugeras, D. P. Arovas, M. M. Fogler, F. Guinea, S. Roche, M. Goiran, and B. Raquet, Phys. Rev. Lett. **107**, 126806 (2011).
- ¹⁸ S. H. Jhang, M. F. Craciun, S. Schmidmeier, S. Tokumitsu, S. Russo, M. Yamamoto, Y. Skourski, J. Wosnitza, S. Tarucha, J. Eroms, and C. Strunk, Phys. Rev. B **84**, 161408 (2011).
- ¹⁹ S. H. R. Sena, J. M. Pereira, F. M. Peeters, and G. A. Farias, Phys. Rev. B **84**, 205448 (2011).
- ²⁰ E. A. Henriksen, D. Nandi, and J. P. Eisenstein, Phys. Rev. X **2**, 011004 (2012).
- ²¹ M. Koshino and E. McCann, Phys. Rev. B **81**, 115315 (2010), Phys. Rev. B **79**, 125443 (2009).
- ²² S. Yuan, R. Roldán, and M. I. Katsnelson, Phys. Rev. B **84**, 125455 (2011).
- ²³ F. Guinea, A. H. C. Neto, and N. M. R. Peres, Phys. Rev. B **73**, 245426 (2006).
- ²⁴ H. Min and A. H. MacDonald, Phys. Rev. B **77**, 155416 (2008); Prog. Theor. Phys. Suppl. **176**, 227 (2008).
- ²⁵ M. Koshino and E. McCann, Phys. Rev. B **80**, 165409 (2009); Phys. Rev. B **81**, 125304 (2010).
- ²⁶ A. A. Avetisyan, B. Partoens, and F. M. Peeters, Phys. Rev. B **81**, 115432 (2010).
- ²⁷ F. Guinea, A. H. C. Neto, N. M. R. Peres, Solid State Comm. **143**, 116 (2007).
- ²⁸ M. Koshino, T. Ando, Phys. Rev. B **76**, 085425 (2007).
- ²⁹ E. McCann and V. I. Falko, Phys. Rev. Lett. **96**, 086805 (2006).
- ³⁰ M. Ezawa, J. Phys. Soc. Jpn **76**, 094701 (2007).
- ³¹ M. F. Craciun, S. Russo, M. Yamamoto, J. B. Oostinga, A. F. Morpurgo, and S. Tarucha, Nature Nanotech. **4**, 383 (2009).
- ³² M. Koshino and E. McCann, Phys. Rev. B **79**, 125443 (2009).
- ³³ W. Bao, L. Jing, J. Velasco Jr, Y. Lee, G. Liu, D. Tran, B. Standley, M. Aykol, S. B. Cronin, D. Smirnov, M. Koshino, E. McCann, M. Bockrath and C. N. Lau, Nature Physics **7**, 948 (2011).
- ³⁴ M. S. Dresselhaus and G. Dresselhaus, Adv. Phys. **51**, 1 (2002).
- ³⁵ R. Ma, L. Sheng, R. Shen, M. Liu and D. N. Sheng, Phys. Rev. B **80**, 205101 (2009); R. Ma, L. Zhu, L. Sheng, M. Liu, D. N. Sheng, Europhys. Lett. **87**, 17009 (2009).
- ³⁶ D. N. Sheng, L. Sheng, and Z. Y. Weng, Phys. Rev. B **73**, 233406 (2006).
- ³⁷ M. Jonson and S. M. Girvin, Phys. Rev. B **29**, 1939 (1984).
- ³⁸ H. Oji, J. Phys. C **17**, 3059 (1984).
- ³⁹ Different literatures may have a sign difference due to different conventions.
- ⁴⁰ J. M. Ziman, *Electrons and Phonons: The Theory of Transport Phenomena in Solids* (Oxford University Press, Oxford, 1963).
- ⁴¹ C. H. Lui, Z. Q. Li, K. F. Mak, E. Cappelluti and T. F. Heinz, Nature Physics, **7**, 944 (2011).
- ⁴² L. Hao, T. K. Lee, Phys. Rev. B **82**, 245415 (2010).
- ⁴³ B. A. Bernevig, T. L. Hughes, H. Chen, C. Wu, and S. C. Zhang, Int. J. Mod. Phys. B **20**, 3257 (2006).